Tuning magnetic coercivity with external pressure in iron-rhenium based ferrimagnetic double perovskites

C. A. Escanhoela, Jr., G. Fabbris, F. Sun, C. Park, J. Gopalakrishnan, K. Ramesha, E. Granado, N. M. Souza-Neto, M. van Veenendaal, and D. Haskel

Phys. Rev. B **98**, 054402 — Published 2 August 2018

DOI: 10.1103/PhysRevB.98.054402

Tuning magnetic coercivity with external pressure in iron-rhenium based ferrimagnetic double perovskites

C. A. Escanhoela Jr.,[1,2] G. Fabbris,[2] F. Sun,[2,3] C. Park,[4] J. Gopalakrishnan,[5] K. Ramesha,[5,*] E. Granado,[6] N. M. Souza-Neto,[1] M. van Veenendaal,[7,2,†] and D. Haskel[2,‡]

[1] *Brazilian Synchrotron Light Laboratory (LNLS), Campinas, SP 13083-970, Brazil*
[2] *Advanced Photon Source, Argonne National Laboratory, Argonne IL 60439*
[3] *Center for High Pressure Science and Technology Advanced Research (HPSTAR), Shanghai 201203, China*
[4] *HPCAT, Carnegie Institution of Washington, Argonne, Illinois 60439, USA*
[5] *Solid State and Structural Chemistry Unit, Indian Institute of Science, Bangalore 560012, India*
[6] *"Gleb Wataghin" Institute of Physics, University of Campinas-UNICAMP, Campinas, São Paulo 13083-859, Brazil*
[7] *Department of Physics, Northern Illinois University, De Kalb, Illinois 60115, USA*

We studied the effect of physical pressure on the electronic and magnetic properties of ferrimagnetic double perovskites A_2FeReO_6 (A=Ca, Ba) using Re $L_{2,3}$ edge x-ray absorption spectroscopy and powder diffraction measurements. Volume compression is shown to dramatically increase the magnetic coercivity (H_c) in polycrystalline samples of both compounds with $\Delta H_c/\Delta V \sim$ 150-200 Oe/Å^3. A nearly eight-fold increase in H_c, from 0.2 T to 1.55 T, is obtained in Ba_2FeReO_6 at P=29 GPa. While no signs of structural phase transitions are seen in either sample to $\sim$ 30 GPa, the structural data points to a pressure-driven increase in tetragonal distortion of ReO_6 octahedra. A sizable but pressure-independent Re orbital-to-spin magnetic moment ratio is observed, pointing to the critical role of spin-orbit interactions at Re sites. We present a $j_{\rm eff}$ description of the electronic structure that combines effects of crystal field and spin-orbit coupling on the Re $5d^2$ orbitals and use this description to provide insight into the pressure-induced enhancement of magnetic anisotropy.

I. INTRODUCTION

The versatility afforded by combining different transition metal (TM) ions at the B and B′ sites of ordered double perovskites $A_2BB'O_6$ (A is an alkaline ion) provides a prolific ground for exploration of novel quantum states and properties[1–7]. This is particularly promising for combinations of TM ions belonging to different rows of the periodic table. For example, the combination of first-row TM ions (localized $3d$ electrons and strong local magnetic moments) at B sites, with the more delocalized $5d$ electrons of heavy third-row TM ions (strong spin-orbit interactions) at B′ sites, can lead to high magnetic ordering temperatures and enhanced anisotropy[8–16]. While oxygen-mediated exchange interactions between $3d$ TM ions in corner-shared TMO_6 octahedra are rather well understood in terms of Goodenough-Kanamori (GK) rules[17–20], the understanding of oxygen mediated $3d$-$5d$ interactions is less developed[21–24]. The disparate energy scales of crystal field (1-3 eV), Coulomb interaction $U - J_H$ where U is on-site Coulomb repulsion and J_H is Hund's coupling (1-7 eV), and spin-orbit interactions (0.01-0.5 eV) at $3d$ and $5d$ sites challenges our understanding of indirect exchange interactions in these systems but presents an opportunity to tailor transport and magnetic properties[25,26]. The extended nature of $5d$ orbitals, while favoring exchange interactions, may require going beyond first neighbor exchange as well as inclusion of direct exchange pathways in microscopic models of magnetic interactions.[27,28].

A case in point is that of double perovskites A_2FeReO_6 (A = Ba, Sr and Ca) and Sr_2FeMoO_6, which are ferrimagnets with high degree of spin polarization of conduction/valence electrons and high magnetic ordering temperature (300-550 K)[29–34], hence good candidate materials for use as spin polarizers/analyzers in spintronic devices[35–38]. A major difference in magnetic properties in going from Mo (second row, $4d$ element) to Re (third row $5d$ element) at B′ sites is that the Re-based double perovskites are magnetically hard while the Mo-based double perovskites are magnetically soft[29,39–41]. This points to the importance of spin-orbit interactions in the heavy Re ions and identifies the Re sublattice as the dominant source of magnetic anisotropy in the Re-based double perovskites which are the focus of the current study.

Choice of A-site ion has a dramatic effect on the transport and magnetic properties of A_2FeReO_6. The larger Ba cation leads to a cubic crystal structure at ambient temperature and metallic behavior, while the smaller Ca cation leads to a lower symmetry monoclinic structure with insulating response[42–46]. The latter also displays higher Curie temperature (T_c = 540 K) and coercivity (H_c = 9 kOe) indicative of stronger exchange interactions and larger magnetic anisotropy in the distorted crystal structure. The monoclinic structure of Ca_2FeReO_6 (CFRO) features rotations of FeO_6 and ReO_6 octahedra around b- and c- axes resulting in large deviation in Fe-O-Re bonding angle away from 180°(to 156°)[32,47,48]. These rotations decrease the $pd\pi$ hopping that dominates transport in the unrotated structure leading to the observed insulating behavior[2,47,49]. The lowering of symmetry leads to a tetragonal distortion of the ReO_6 octahedra and enhanced magnetic anisotropy relative to the Ba compound.

Although the Ba_2FeReO_6 (BFRO) compound is cubic at room temperature, neutron powder diffraction and high resolution synchrotron x-ray powder diffraction data show emergence of tetragonality at low

temperatures[50,51]. The lowering of symmetry coincides with the onset of magnetic ordering and the tetragonal distortion grows together with the magnetic order parameter as a result of magneto-elastic coupling[2,32,47,50,52].

The pronounced effect of *chemical* pressure by A-site substitution on the structural, transport and magnetic properties, including magnetic anisotropy, makes double perovskites A_2FeReO_6 interesting subject materials for high pressure studies. In this paper, we explore the use of *physical* pressure as a tool to modify the structure of these double perovskites in a controlled manner, allowing us to establish correlations between lattice changes and electronic properties, particularly magnetic anisotropy. Using x-ray spectroscopic and structural probes in a diamond anvil cell we find a substantial increase in the coercivity of BFRO and CFRO samples under pressure. Both compounds exhibit a similar rate of coercivity increase with change in unit cell volume, of order 150-200 Oe/ Å^3. X-ray diffraction shows a clear increase in the tetragonal distortion of ReO_6 octahedra under pressure for CFRO. Limitations in angular resolution and hydrostaticity only allow us to place an upper limit to the degree of tetragonal distortion in BFRO, a distortion that remains unresolved in our room temperature XRD data. A j_{eff} theoretical model is developed for the Re $5d^2$ orbitals, pointing to a "high-spin", spin-orbit coupled ground state stabilized by Hund's coupling and explaining the unique spectroscopies signatures in the x-ray absorption data. The model also shows how an increase in the tetragonal crystal field under pressure can be responsible for the enhanced single ion anisotropy in the presence of strong spin-orbit coupling. X-ray magnetic circular dichroism sum rules show the presence of sizable orbital magnetism at Re sites, a critical ingredient of single-ion anisotropy. The orbital magnetization does not increase with pressure, and the enhanced coercivity is rooted in an enhanced tetragonal distortion under pressure. A derivation of the anisotropy constant in the $5d^2$ configuration within a j_{eff} model points to the surprising result that a reduction in the effective spin-orbit interaction may cooperate with an enhanced tetragonal distortion in increasing the single-ion anisotropy.

The paper is organized as follows: SectionII describes experimental methods. SectionIII presents XANES and XMCD results pointing to the relevance of spin-orbit interactions at Re sites. A theoretical description of the Re $5d^2$ configuration based on a spin-orbit coupled j_{eff} model is presented which explains the spectroscopic signatures in the x-ray absorption data. SectionIV presents XMCD and XRD results on the magnetic and structural response to pressure and derives correlations between changes in coercivity, unit cell volume, and degree of tetragonality. A theoretical derivation of the origin of magnetic anisotropy within a j_{eff} model is also presented in this section. SectionV summarizes the results. Finally, an appendix provides additional details on theoretical calculations of expectation values of orbital, spin, and magnetic dipole moments derived within the j_{eff} model used to describe the Re $5d^2$ configuration.

II. EXPERIMENTAL METHODS

Polycrystalline BFRO and CFRO samples were grown by solid state reaction methods as described in Refs. 50,53. X-ray absorption near edge structure (XANES) and x-ray magnetic circular dichroism (XMCD) measurements were carried out across the Re $L_{2,3}$ edges (10.5-12 keV) at beamline 4-ID-D of the Advanced Photon Source (APS), Argonne National Laboratory. A pair of Pd mirrors at 3.1 mrad incidence angle, together with detuning of the second crystal in a double crystal Si (111) monochromator, was used to reject higher energy harmonic contamination in the x-ray beam. High pressure XANES and XMCD data were collected on dispersed powder samples (3-5 μm powder size) at T=10 K in transmission geometry using thin (thick) Si photodiodes as detectors of incident (transmitted) x-ray intensity, respectively. XMCD measurements were done in fast helicity switching mode (13.3 Hz) using a 500 μm-thick diamond (111) phase retarder[54,55]. The related modulation in absorption coefficient was measured with a lock-in amplifier[54–58]. XMCD lock-in detected signals were scaled to absolute percentages of isotropic absorption edge jumps by comparing to XMCD data obtained at the Re L_2 edge without lock-in detection. XMCD data was corrected for degree of circular polarization which was 95(90)% at L_3(L_2) edges, respectively. XMCD measurements were carried out for magnetic field direction along and opposite the incident photon wave vector in order to remove any artifacts of non-magnetic origin. An external magnetic field of H = $\pm$4 T was used to saturate the magnetization at all pressures.

Two types of diamond anvil cells and cryomagnets were used in the measurements. The BFRO data were collected using a non-magnetic mini-DAC (manufactured by D'anvils) mounted in a helium flow variable temperature insert that loads into the 1″ bore of a cryogen free magnet. Pressure was applied manually and calibrated at room temperature (RT). Pressure values reported for the BFRO sample are therefore RT values. Careful characterization of the response of the sample pressure in the mini-DAC to cooling has shown that pressure remains stable within $\sim$ 10% of RT values. The CFRO data were collected using a non-magnetic, CuBe diamond anvil cell (Diacell OmniDAC-LT model, Almax Easylabs) fitted with a He gas membrane allowing in-situ pressure change at low temperatures. The DAC mounts on a variable temperature insert in the 3″ bore of a cryomagnet and is cooled by cold He gas leaked from the magnet reservoir into the sample tube. The diamond anvil cells used in both cases featured a partially perforated diamond anvil (150 μm remaining wall thickness) opposite a mini-anvil (0.8 mm in height) placed on top of a fully perforated anvil to minimize x-ray absorption in the diamond anvils[54]. Culet diameter was 300 μm.

Powders of BFRO (CFRO) were loaded into a 120 μm diameter hole in a rhenium gasket pre-indented to 30 μm, together with ruby spheres for ex-situ (in-situ) pressure calibration[59] and 4:1 methanol-ethanol mixture as quasi-hydrostatic pressure-transmitting medium. Energy dependent XANES/XMCD measurements were carried out across Re $L_{2,3}$ edges while field-dependent (coercivity) measurements were performed at a fixed x-ray energy that maximizes the Re L_2 edge XMCD signal. For CFRO, field-dependent XMCD data was collected in the H = ±2 T range after sample was saturated at H = ±4 T. The 4:1 methanol-ethanol pressure medium solidifies at around 120 K at ambient pressure[60] hence the powder sample preserves a random orientation under application of magnetic field in the XMCD measurements at 10 K.

The powder x-ray diffraction (XRD) experiments at high-pressure were performed at HP-CAT beam line 16-BM-D of the Advanced Photon source using a symmetric DAC (Princeton). A boron carbide conical seat that is semi-transparent to 30 keV x-ray radiation was used on the exit side of the DAC to extend the angular range of the XRD pattern in the CFRO measurements. The angular range in the BFRO measurements was limited by a opaque tungsten-carbide seat used on the exit side. A partially perforated diamond anvil opposite a full anvil with culet size of 300 μm was used in the CFRO measurements; two full anvils were used in the BFRO measurements. A 130 μm diameter hole in a rhenium gasket pre-indented to 50 μm was filled with dispersed powder (3-5 μm powder size) as well as Au powder and ruby spheres for *in-situ* pressure calibration. A 4:1 methanol-ethanol mixture was used as pressure-transmitting medium. The measurements were carried out at room temperature and pressure was increased manually. XRD patterns were recorded with a MAR345 image plate and converted into 1D plots. XRD data were fitted using the Le Bail method[61] available within the GSASII package[62].

III. SPIN-ORBIT INTERACTION IN Re 5d ORBITALS

A. XANES and XMCD experimental results

The pressure-dependent normalized XANES data at Re $L_{2,3}$ edges collected at $T = 10$ K on both BFRO and CFRO samples are shown in Figs. 1(a) and (b). The Re XANES spectra ($2p \rightarrow 5d$ transition) for both samples have the same leading-edge positions and double-peak "white line" structure at both edges. The white line peak splitting of 3.0 eV is a measure of the octahedral crystal-field splitting of the d orbitals into t_2 and e states, both of which carry empty (hole) states in a Re $5d^2$ configuration.

Pressure-dependent XMCD spectra for both compounds are shown in Figure 1(c,d). The large difference in XMCD intensity at L_3 and L_2 edges is indicative of a sizable orbital angular momentum contribution to the magnetic moment carried by Re $5d$ states[63–65]. The dominant, negative XMCD signal at the L_2 edge indicates that the magnetic moment at Re sites is aligned antiparallel to the applied field (hence also to the Fe moment) as expected from the ferrimagnetic nature of these compounds (Fe^{3+} ions with a high spin $5d^5$ configuration have a larger magnetic moment than Re^{5+} ions with $5d^2$ configuration; their coupling is antiferromagnetic)[47,49,53,66]. The circular dichroism has the unusual feature that almost all the intensity is in the L_2 edge, see Fig. 1(c) and (d). While the spectral features can be well reproduced with density functional theory[4], we demonstrate in the next subsection that the essential features are consistent with a $j_{\rm eff}$ model which is commonly used to describe iridates. An approximation underlying this model is that the cubic crystal field is sufficiently large that we can focus on the t_2 states[67]. The low-energy physics is then dominated by the spin-orbit interaction. We show that, in order to find the Re $5d^2$ ground state, one also has to consider the Coulomb exchange or Hund's coupling within crystal field split $j_{\rm eff}$ states.

XMCD sum rules were used to obtain Re spin and orbital magnetic moments, their relative orientation, and their pressure dependence. We have computed these quantities both neglecting and including the magnetic dipole operator (T_z) that enters the spin sum rule[63–65]. In the latter case, $T_z/S_z = 0.37$ was derived from atomic multiplet calculations described in section III B. Since XMCD measurements and related sum rules analysis were carried out at low temperature (10 K), temperature effects on the expectation value of S_z and T_z are neglected[69]. The magnetic moments were calculated using $n_h = 8$ based on the $5d^2$ configuration (a derivation of the magnetic dipole term within the $j_{\rm eff}$ model is given in the Appendix). The results, summarized in Table I,

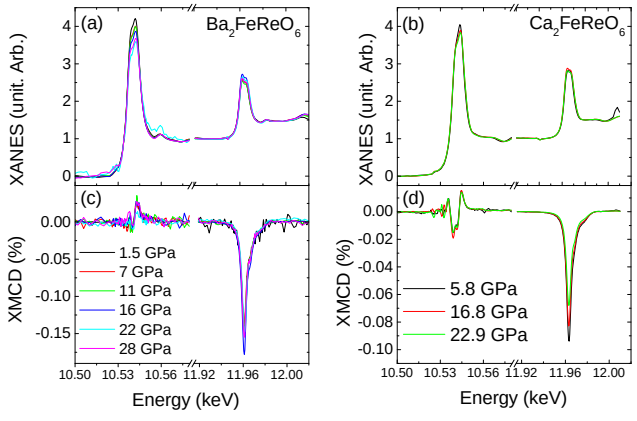

FIG. 1: Nomalized Re $L_{2,3}$-edge XANES and XMCD spectra for BFRO (a,c) and CFRO (b,d) double perovskites measured up to 30 GPa at T=10 K.

TABLE I: Electronic properties of the Re 5d orbitals in BFRO and CFRO samples extracted from XMCD and XANES data at T=10 K for different pressures. The Re orbital moment ($m_l = -\langle L_z \rangle$), spin moment ($m_s = -2\langle S_z \rangle$), and total magnetic moment (m_{tot}) were obtained for 5d hole occupancy $n_h = 8$. Inclusion of the magnetic dipole term T_z in the spin sum rule leads to a reduction in the absolute value of derived spin and total magnetic moments (values in square brackets). When T_z is neglected, magnetic moment values are in reasonable agreement with results obtained in ambient pressure XMCD studies, once normalized to the different hole occupancies used in the respective analyses. Note that m_l/m_s is independent of n_h but it is affected by the T_z contribution.

	Pressure(GPa)	$m_s(\hbar)$	m_l ($\hbar$)	m_l/m_s	$m_{\rm tot}(\hbar)$	BR
	1.5(5)	-0.94(2) [-0.41(1)]	0.27(2)	-0.29(2) [-0.66(2)]	-0.67(2) [-0.14(2)]	2.8
	7.9(5)	-0.88(2) [-0.38(1)]	0.26(1)	-0.29(2) [-0.68(2)]	-0.62(2) [-0.12(2)]	2.6
	10.9(5)	-0.91(2) [-0.39(1)]	0.26(1)	-0.28(2) [-0.65(2)]	-0.66(2) [-0.14(2)]	2.9
BFRO	16.3(5)	-1.10(2) [-0.47(1)]	0.32(2)	-0.29(2) [-0.67(2)]	-0.78(2) [-0.16(2)]	2.3
$n_h = 8$	22.3(10)	-0.89(2) [-0.39(2)]	0.24(2)	-0.27(2) [-0.62(2)]	-0.65(2) [-0.15(2)]	2.3
	28.5(10)	-0.95(2) [-0.41(1)]	0.26(2)	-0.27(2) [-0.63(2)]	-0.69(2) [-0.15(2)]	2.1
Ref.[30]($n_h = 8.2$)	1 bar	-0.99	0.28	-0.283	-0.71	
Ref.[68]($n_h = 5.3$)	1 bar	-0.56	0.15	-0.27	-0.41	
Ref.[50]($n_h = 5.5$)	1 bar	-0.64	0.19	-0.294	-0.45	
	5.9(1)	-0.76(1) [-0.33(1)]	0.18(2)	-0.24(1) [-0.55(2)]	-0.58(1) [-0.15(1)]	2.2
CFRO	17.7(10)	-0.66(1) [-0.28(1)]	0.16(2)	-0.24(1) [-0.57(2)]	-0.50(2) [-0.12(1)]	2.1
$n_h = 8$	22.9(20)	-0.56(1) [-0.24(1)]	0.13(2)	-0.24(1) [-0.55(2)]	-0.43(2) [-0.11(1)]	2.1
Ref.[30]($n_h = 7.8$)	1 bar	-1.15	0.39	-0.34	-0.76	
Ref.[68]($n_h = 5.3$)	1 bar	-0.47(1)	0.16(4)	-0.34(3)	-0.31(1)	

show sizable Re orbital magnetic moments in both samples. Spin and orbital moments are aligned antiparallel to each other as expected from Hund's rules for a less than half-filled 5d band (orbital moment aligned parallel to Fe spin moment and to external magnetic field). When T_z is neglected, the derived values of the spin moments given in Table I are in reasonable good agreement with previous reports (work at ambient pressure) which did not include the magnetic dipole term in the spin sum rule[30,46,50,68,70,71] provided the moment values are corrected for the number of holes used in the respective analyses (moment values scale linearly with n_h; this also applies to the orbital moment values). The m_l/m_s ratios are independent of n_h but depend on T_z. When T_z is neglected, m_l/m_s ratios agree reasonably well with previous reports that neglected T_z. The analysis shows somewhat larger m_l/m_s ratio for BFRO than CFRO, perhaps a result of increased covalency/bandwidth in the chemically compressed CFRO structure. A smaller m_l/m_s ratio in CFRO is consistent with a reduced isotropic branching ratio (BR=I(L_3)/I(L_2), where I($L_{2,3}$) are white line intensities in the isotropic XANES data). This is because the BR relates to the expectation value of the angular part of the S-O interaction, as discussed in detail in section III B. Both structures retain a nearly unchanged m_l/m_s ratio under pressure. The CFRO sample shows a reduction in m_l with pressure outside error bars (27 $\pm$ 16% at highest pressure) but a similar reduction in m_s leads to a pressure-independent m_l/m_s ratio.

B. A $j_{\rm eff}$ theoretical description of spin-orbit coupled Re 5d orbitals

The splitting of the 5d states under the various interactions can be directly understood from group-theoretical considerations. The local electronic structure of 5d transition-metal compounds is characterized by a competition between the spin-orbit interaction and the local crystal fields[1,2,4,67]. The strongest interaction is the cubic crystal field ($10Dq \approx 3$ eV) that splits the 5d

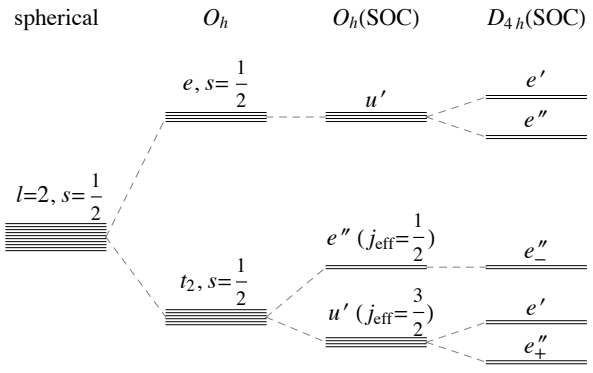

FIG. 2: Schematic figure of the branching of the 5d orbital when lowering the symmetry from spherical to octahedral (O_h) in the absence of spin-orbit coupling. The next to level schemes show the effect of coupling the orbital and spin degrees of freedom in octahedral symmetry, O_h (SOC), followed by the effect of the tetragonal splitting D_{4h} (SOC).

orbitals (with angular momentum $l = 2$) into twofold-degenerate e and threefold-degenerate t_2 states, using Mulliken notation[72]. The splitting is indicated by O_h in Fig. 2. Pentavalent rhenium has a t_2^2 configuration. However, due to the strong spin-orbit interaction, $\zeta \mathbf{L}\cdot\mathbf{S}$ with $\zeta \cong 0.3$-0.4 eV, it is necessary to couple the orbital and spin degrees of freedom. The twofold-degenerate spin space with spin projections $\pm\frac{1}{2}$ is denoted by the irreducible representation e'. The high-lying e states do not split under the spin-orbit interaction and give the fourfold degenerate state $u' = e \otimes e'$ after coupling the irreducible representations of the orbital (e) and spin parts (e'), see the states denoted by O_h (SOC) in Fig. 2. The spin-orbit interaction, however, will split the t_2 states. One can view the orbital part of the three-fold degenerate t_2 irreducible representation as an effective angular momentum $l_{\text{eff}} = 1$. Note that the projected angular momentum of l_{eff} is opposite to the real angular momentum, *i.e.* $m_{\text{eff}} = -m$. The spin-orbit interaction couples this to the spin forming total angular momenta $j_{\text{eff}} = \frac{1}{2}, \frac{3}{2}$. In octahedral symmetry,[72] the coupling between the orbital t_2 and the spin e' is indicated as $t_2 \otimes e' = e'' \oplus u'$, where e and u, are two- and fourfold degenerate representations, respectively, see O_h (SOC) in Fig. 2. Pressure tuning affects the tetragonal distortion, which is important for understanding the magnetic anisotropy that will be discussed in the next section. The distortion further lowers the symmetry to D_{4h} and the fourfold degenerate u' further splits into two two-fold degenerate e' and e'' irreducible representations. In summary, the splitting in going from spherical to octahedral to tetragonal symmetry ($SO_3 \rightarrow O_h \rightarrow D_{4h}$) is $2 \otimes \frac{1}{2} \rightarrow (t_2 \oplus e) \otimes e' = (u' \oplus e'') \oplus u' \rightarrow (e' \oplus e'' \oplus e'') \oplus (e' \oplus e'')$, see Fig. 2. For rhenium, we are primarily concerned with the first group arising from the octahedral t_2 states. In order to distinguish the two e'' irreducible representations, a subscript $\pm$ will be added to indicate the effective total angular momentum $j_{\text{eff}}^{\pm} = 1 \pm \frac{1}{2} = \frac{3}{2}, \frac{1}{2}$ that they belong to. The t_2 states therefore branch from octahedral to tetragonal symmetry as $t_2 \otimes e' = u' \oplus e''_- \rightarrow e' \oplus e''_+ \oplus e''_-$. Note that depending on the size of the atomic parameters and band width effects, there are a number of possible ground states.

The conventional components of the t_2 states in octahedral symmetry are the real (or tesseral) harmonics xy, yz, and zx. The effect of the spin-orbit interaction is to create finite angular momentum states out of the yz and zx orbitals, which are a linear combination of the spherical harmonics $Y_{2,\pm1}(\theta,\varphi)$. The spherical harmonics can be written in terms of the tesseral harmonics as

$$|\pm 1,\sigma\rangle = \mp\frac{1}{\sqrt{2}}(|zx,\sigma\rangle \pm i|yz,\sigma\rangle), \tag{1}$$

where $\sigma = \pm\frac{1}{2}$ is the spin. The wavefunctions $|m,\sigma\rangle$ are expressed in terms of the projected angular momentum m. In this convention, the xy orbital corresponds to the $m = 0$ component of the $l_{\text{eff}} = 1$ states. In the limit of a large cubic field $10Dq$, we can focus on the states arising from t_2, *i.e.* e''_-, e''_+ and e'. Let us start with

$$|e''_-, \pm\frac{1}{2}\rangle = \sin\theta|xy, \pm\frac{1}{2}\rangle \pm i\cos\theta|\mp 1, \mp\frac{1}{2}\rangle. \tag{2}$$

These states are the well-known $j_{\text{eff}} = \frac{1}{2}$ states that are responsible for the low-energy behavior in the iridates[67]. The irreducible representation e''_- is indicated with a minus sign, since the effective orbital and spin are coupled antiparallel. The choice of the spin components of e''_- corresponds to that of the j_{eff} notation.

The value of the coefficients depends on the relative strengths of the interactions:[67]

$$\theta = \frac{1}{2}\arctan\frac{2\sqrt{2}\zeta}{\zeta - 2\varepsilon_{xy}}, \tag{3}$$

where ζ is the strength of the spin-orbit interaction $\zeta\mathbf{L}\cdot\mathbf{S}$ and ε_{xy} gives the change in energy of the xy orbital, $E_{xy} = -4Dq + \varepsilon_{xy}$, due to the tetragonal distortion. In the limit $\varepsilon_{xy} = 0$, $\cos\theta = \sqrt{2/3}$ and $\sin\theta = 1/\sqrt{3}$ and the states are independent of the value of the parameters. In the opposite limit $\zeta \ll \varepsilon_{xy} \ll 10Dq$, $\theta \rightarrow 0$.

Whereas the e''_- or $j_{\text{eff}} = \frac{1}{2}$ states are important for iridates, these states are predominantly empty in the Rhenium compounds, where the electrons are in the $j_{\text{eff}} = \frac{3}{2}$ (e' and e''_+ in tetragonal symmetry). The e''_+ eigenfunctions contain the same basis functions as e''_-,

$$|e''_+, \pm\frac{1}{2}\rangle = \cos\theta|xy, \pm\frac{1}{2}\rangle \mp i\sin\theta|\mp 1, \mp\frac{1}{2}\rangle. \tag{4}$$

Additionally, there are two eigenstates that are independent of the parameter values

$$|e', \pm\frac{1}{2}\rangle = |\mp 1, \pm\frac{1}{2}\rangle. \tag{5}$$

For A_2FeReO_6, the apical rhenium-oxygen distance is less than that in the basal plane[47]. Within a crystal-field picture, that lowers the energy of the xy orbitals with respect to yz/zx ($\varepsilon_{xy} < 0$). Since e''_+ has xy character, this state is expected to be lower in energy than e' as depicted in Fig. 2.

For Re^{5+}, the two electrons are expected to be in the $j_{\text{eff}} = \frac{3}{2}$ states or, equivalently in tetragonal symmetry, the e' and e''_+ states. There are a number of different possibilities. The clearest way to distinguish the different possible ground states is the circular dichroic spectra. The integrated intensities at a particular spin-orbit split edge can be written in terms of coupled tensors as[64,65,73]

$$\begin{aligned} I^1(j^{\pm}) &= (j^{\pm}+1)\langle \underline{w}_z^{101}\rangle \pm \frac{1}{3}\left(\langle \underline{w}_z^{011}\rangle + 2\underline{w}_z^{211}\rangle\right) \\ &= -\frac{j^{\pm}+1}{2}\langle L_z\rangle \mp \frac{1}{3}\left(2\langle S_z\rangle + 7\langle T_z\rangle\right) \end{aligned} \tag{6}$$

where $j^{\pm} = 1 \pm \frac{1}{2} = \frac{3}{2}, \frac{1}{2}$ refers to the total angular momentum of the $2p$ core hole. The coupled tensor $\underline{w}_z^{xyz}$ consists of orbital and spin operators (of rank x and y,

respectively) coupled to a total operator of rank z. For x-ray circular dichroism, the total rank is $z = 1$ and the coupled tensors correspond to the angular momentum $L_z = -2w_z^{101}$, the spin $S_z = -\frac{1}{2}w_z^{011}$, and the magnetic dipole moment $T_z = -\frac{2}{7}w_z^{211}$, using electron operators. Using the expressions for the eigenfunctions above, the expectation values of the coupled tensors can be evaluated, see the Appendix, and the intensities of each orbital at the two absorption edges can be obtained. For the different states arising from the t_2 orbitals, we find

$$\begin{aligned} I^1_{e''_+,\pm\frac{1}{2}}(\frac{3}{2}) &= -I^1_{e''_-,\pm\frac{1}{2}}(\frac{3}{2}) = \pm\left(\cos 2\theta + \frac{1}{\sqrt{2}}\sin 2\theta\right) \\ I^1_{e''_\alpha,\pm\frac{1}{2}}(\frac{1}{2}) &= \mp\left[\frac{3}{4} + \alpha\left(\frac{1}{4}\cos 2\theta + \frac{1}{\sqrt{2}}\sin 2\theta\right)\right] \end{aligned} \quad (7)$$

where $\alpha = \pm 1$, and

$$I^1_{e',\pm\frac{1}{2}}(j^\pm) = \pm(\frac{j^\pm}{2} + \frac{1}{4}). \quad (8)$$

Let us consider the limit of a small tetragonal distortion ($\varepsilon_{xy} \to 0$). The important orbitals for Re^{5+} are e' and e''_+ arising from the $j_{\rm eff} = \frac{3}{2}$ states. The integrated dichroic absorption intensities for these states are

$$I^1_{e',\pm\frac{1}{2}}(\frac{3}{2}) = \mp 1, \qquad I^1_{e''_+,\pm\frac{1}{2}}(\frac{3}{2}) = \pm 1 \quad (9)$$

at the L_3 edge, and

$$I^1_{e',\pm\frac{1}{2}}(\frac{1}{2}) = \mp\frac{1}{2}, \qquad I^1_{e''_+,\pm\frac{1}{2}}(\frac{1}{2}) = \mp\frac{3}{2} \quad (10)$$

at the L_2 edge. First, we note that the configurations e'^2 and e''^2_+ show no dichroism and can be ruled out. For the $e' \uparrow e''_+ \uparrow$ configuration, this gives integrated intensities $I^1(\frac{3}{2}) = 0$ and $I^1(\frac{1}{2}) = -2$, whereas for the $e' \uparrow e''_+ \downarrow$ configuration, one obtains $I^1(\frac{3}{2}) = -2$ and $I^1(\frac{1}{2}) = 1$. Note that the dichroism changes sign for a spin reversal. Since experiment tells us that the dichroic signal is small at the L_3 edge that leaves us with the $e' \uparrow e''_+ \uparrow$ configuration. As shown in the Appendix, the expectation values for the spin are $\frac{1}{2}$ and $\frac{1}{6}$ (in units $\hbar$) for $e' \uparrow$ and $e''_+ \uparrow$ states, respectively. Therefore, the real spins in these two states are also predominantly parallel in the $e' \uparrow e''_+ \uparrow$ configuration indicating a tendency towards the formation of a local moment by the Coulomb interactions. This is essentially a Hund's rule type ground state. The total expection value of the spin is therefore $\langle S_z\rangle = \frac{2}{3}$. When increasing the tetragonal distortion, the value increases up to the maximum $\langle S_z\rangle = 1$. The corresponding angular momentum values are $\langle L_z\rangle = -4/3 \to -1$ from zero to large tetragonal distortion.

These conclusions are also confirmed by an atomic multiplet calculation[73], see Fig. 3. The calculation was done for a Re^{5+} ion. Good agreement is obtained using a spin-orbit interaction strength of $\zeta = 0.35$ eV and a cubic crystal field of $10Dq = 3.8$ eV. The Coulomb exchange parameters are strongly screened and scaled down to 20% of their Hartree-Fock value. The tetragonal distortion is small and does not really affect the spectral line shape and intensities. These parameters clearly reproduce the isotropic spectrum giving the splitting of the two peaks in the white line and the correct branching ratio. Additionally, the dichroic intensity comes primarily from the L_2 edge. This supports the notion that the two electrons are in the $j_{\rm eff} = \frac{3}{2}$ states and that the Coulomb interaction is crucial for maximizing the spins leading to a finite magnetic moment. For comparison, Figure 3 shows the spectra in the absence of a spin-orbit interaction (dashed lines). In that case, the branching ratio of the isotropic spectra drops to its statistical value ($I^0(\frac{3}{2})/I^0(\frac{1}{2}) = 2$) and the dichroic intensities are equal in magnitude but opposite at the two absorption edges. Again, this is a clear indication that the spin-orbit interaction plays a dominant role in early $5d$ transition-metal compounds. For the numerical calculation, one can also obtain the ground-state expectation values. For the best fit on BFRO, $\langle L_z\rangle = -1.35$ and $\langle S_z\rangle = 0.82$. This is in good agreement with what is expected from a $e' \uparrow e''_+ \uparrow$ ground state in a $j_{\rm eff}$ model. The calculated orbital-to-spin ratio $m_l/m_s = \langle L_z\rangle/2\langle S_z\rangle = 0.82$ somewhat overestimates the experimental values in Table I.

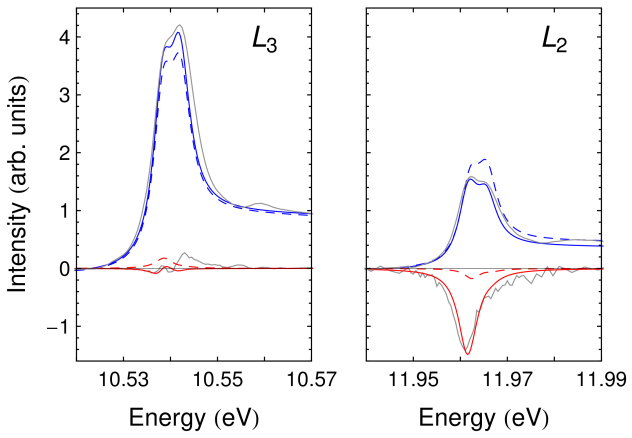

FIG. 3: Comparison of the experimental BFRO spectra (gray) at 1.5 GPa with an atomic multiplet calculation of the isotropic (blue) and circular dichroic (red) x-ray absorption spectra at the L_3 and L_2 absorption edges. The dashed line shows the result in the absence of the spin-orbit interaction.

The integrated spectral weight at the spin-orbit split edges can be understood by analyzing the ground-state expectation value of various operators[74]. Let us first look at the expectation value of the spin-orbit coupling $\langle \mathbf{L}\cdot\mathbf{S}\rangle$ which is of relevance for the interpretation of the isotropic branching ratio, which is given by

$$\frac{I^0(\frac{3}{2})}{I^0(\frac{1}{2})} = \frac{2+r}{1-r} \quad \text{with} \quad r = -\frac{\langle \mathbf{L}\cdot\mathbf{S}\rangle}{\langle n_h\rangle} \quad (11)$$

where $n_h = 8$ is the number of holes $I^0(j^\pm)$ refers to the integrated intensity of the isotropic spectrum at the

spin-orbit-split edge with a total angular momentum $j^{\pm} = \frac{3}{2}, \frac{1}{2}$ (L_3 and L_2 edges, respectively). We have introduced a sign change in r with respect to earlier work[75,76], since we will be considering the spin-orbit coupling for the electrons and not the hole states. Within a $j_{\rm eff}$ framework, the spin-orbit coupling can be obtained via

$$\langle \mathbf{L}\cdot\mathbf{S}\rangle \;=\; -[j^{\pm}_{\rm eff}(j^{\pm}_{\rm eff}+1) - l(l+1) - s(s+1)] = -\frac{1}{2}, 1,$$

with $s = \frac{1}{2}$. The minus sign is needed since the real orbital moment, of relevance for the sum rule, is opposite to the effective orbital moment. Since there are two electrons with $j_{\rm eff} = \frac{3}{2}$, the expectation value is $\langle \mathbf{L}\cdot\mathbf{S}\rangle = 2\times(-\frac{1}{2}) = -1$ giving $r = \frac{1}{8}$. The expected branching ratio is then 2.43. Another aspect that increases the branching ratio is the coupling to the e states that are $10Dq$ higher in energy. This contribution is estimated to be of the order[75,76] $-3\zeta/(10Dq)$ for each of the electrons in the $j_{\rm eff} = \frac{3}{2}$ states. With $\zeta/(10Dq) \cong 0.1$, this increases $\langle \mathbf{L}\cdot\mathbf{S}\rangle$ to -1.6 and the branching ratio to 2.75. This value is close to the experimentally observed branching ratio, see Table I for BFRO, although it overestimates that of CFRO.

With the analytical expressions for the eigenstates, we can estimate the effects of a tetragonal distortion. Since the e' states, see Eq. (5), are unaffected by the tetragonal distortion, $\langle \mathbf{L}\cdot\mathbf{S}\rangle = -\frac{1}{2}$ regardless of ε_{xy}. For the e'' states, we obtain

$$\langle \mathbf{L}\cdot\mathbf{S}\rangle_{e''_{\pm}} = \frac{1}{4} \mp \left(\frac{1}{4}\cos 2\theta + \frac{1}{\sqrt{2}}\sin 2\theta\right) \qquad (12)$$

where $\langle \mathbf{L}\cdot\mathbf{S}\rangle_{e''_{+}} = -\frac{1}{2} \rightarrow 0$ from zero to large tetragonal distortion. Therefore, for the $e' \uparrow e''_{+} \uparrow$ configuration $\langle \mathbf{L}\cdot\mathbf{S}\rangle = -1 \rightarrow -\frac{1}{2}$ for $|\varepsilon_{xy}| = 0 \rightarrow \infty$ (with $|\varepsilon_{xy}| \ll 10Dq$). Therefore, the tetragonal crystal field is unable to entirely quench the spin-orbit coupling. The maximum decrease in branching ratio due solely to the enhanced tetragonal field is 2.47. There are several additional effects that can further reduce the branching ratio as a function of pressure. A stronger change is expected from increased delocalization that causes a mixing of the different $j_{\rm eff}$ levels leading to a reduction of the effective spin-orbit coupling[77]. Additionally, the smaller effective spin-orbit coupling strength combined with a larger cubic field can decrease the mixing of the e with the t_2 orbitals, thereby lowering its contribution to $\langle \mathbf{L}\cdot\mathbf{S}\rangle$.

IV. PRESSURE DEPENDENCE OF MAGNETIC COERCIVITY

A. XMCD hysteresis loops

Element-selective Re hysteresis loops collected at $T = 10$ K at various pressures are shown in Figure 4. Both samples become magnetically harder with increased pressure, the coercivity of BFRO increasing nearly eight-fold between 1.5 and 29 GPa and that of CFRO increasing about three-fold at 23 GPa. We note that the CFRO sample is pre-compressed due to chemical pressure so its volume change is less than in BFRO for a given change in pressure, especially at low pressures (CFRO has higher bulk modulus than BFRO, see Fig. 6(b)). As discussed

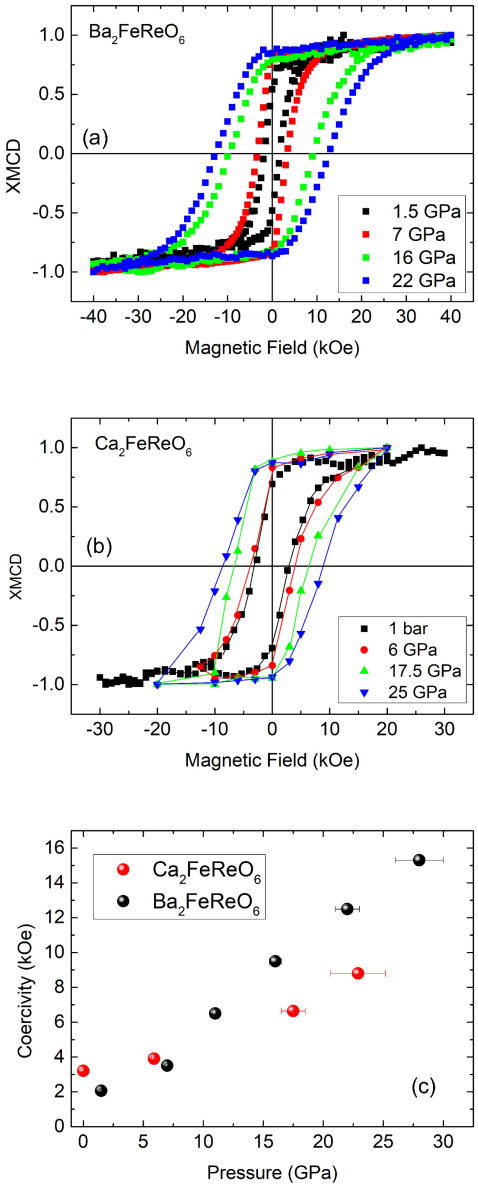

FIG. 4: Element selective (Re) XMCD hysteresis loops at selected pressures measured with x-ray energy tuned to the vicinity of the Re L_2-edge for different pressures for (a) BFRO, and (b) CFRO samples. Loops were normalized to saturation values. Pressure-dependent coercivity, H_c, is shown for both samples in panel (c).

below, the different compressibility of CFRO and BFRO is accounted for in Fig. 7 where coercivity is plotted as a function of unit cell volume yielding similar values of $\Delta H_c/\Delta V$ for CFRO and BFRO. The sizable coercivity of these compounds even at ambient pressure originates in the spin-orbit interaction in $5d$ orbitals of heavy Re ions[29,30,78]. As discussed earlier, that the dominant contribution to magnetic anisotropy arises from the Re sublattice is evident by comparing to the $4d$-analog Sr_2FeMoO_6, which displays coercive fields of only a few Oe[79]. Mössbauer effect measurements also indicate negligible orbital moment contribution in the Fe sublattice of the CFRO compound[30].

The sizable coercivity likely arises from single ion anisotropy at the Re sites, *i.e.*, the combined effect of crystal field, which dictates orbital symmetry, and spin-orbit interaction, which leads to orbital magnetization and couples the spin direction to the lattice structure. *Chemical* pressure also drives a significant increase in coercivity, which correlates with an enhanced m_l/m_s ratio[30]. *Physical* pressure, however, has a negligible effect in m_l/m_s ratio (see Table I), while drastically changing the coercivity. This suggests that the increase in magnetic anisotropy at high pressure is not due to a concomitant increase in the magnitude of the powder-averaged orbital moment $\langle L_z \rangle$. Rather, it indicates that changes in crystal field through lattice distortions may be at the core of the observed increases in coercivity.

B. Structural response

Figure 5 shows XRD patterns under variable pressure collected at room temperature. The cubic $Fm\bar{3}m$ space group was used in Le Bail fits of lattice parameters for the BFRO sample while the monoclinic $P2_1/n$ space group was used for the CFRO sample[32,43,46,47,80]. Limitations in the extent of powder averaging (texturing) due to small probed volume by focused x-ray beam, peak broadening above 10 GPa as a result of pressure gradients in the quasi-hydrostatic pressure medium, together with limited angular range in the case of BFRO prevented us from carrying out reliable Rietveld refinements. The Le Bail fits allow retrieving lattice parameters but do not inform on fractional atomic coordinates[61]. The latter were fixed to their ambient pressure values as given in Refs. 46,47,51. As shown in Figure 6, no discontinuities in lattice parameters or signatures of a structural phase transition were found in either sample in the entire pressure range up to 29 GPa. The measured pressure-volume relationship was fitted to a second-order Birch-Murnaghan equation of state[81,82] yielding structure bulk modulus, included in Fig. 6 (b). The chemically pre-compressed CFRO sample has a smaller compressibility (larger bulk modulus) than the BFRO sample in the measured pressure range. Fitted bulk moduli are comparable with those of other double perovskites. For example, cubic double perovskite Ba_2MgWO_6 has $B_0 = 137$ GPa[83] similar to $B_0 = 152$ GPa for cubic BFRO. Tetragonal double perovskites like Sr_2ZnTeO_6 have typical B_0 values around 200 GPa[84], similar to B_0=189 GPa for CFRO.

As discussed in the next section, non-cubic distortions of the ReO_6 are likely to play a role in the pressure-dependent coercivity, thus we now examine in more detail the structure of each sample. While CFRO retains its monoclinic $P2_1/n$ symmetry to the highest pressure measured, the unit cell contraction however is not uniform: $\Delta a/a \sim -0.06$, $\Delta b/b \sim -0.02$ and $\Delta c/c \sim -0.03$, which points to a potential distortion of the ReO_6 octahedra. As previously stated atomic coordinates could not be extracted from the XRD data; nevertheless, we assume here that the atomic coordinates are pressure independent in order to extract the Re-O distances displayed in Figure 6 (c) and (d). A transition from a compressed (roughly along c axis) to an elongated (within the ab plane) ReO_6 octahedra is observed between 10 and 20 GPa (at room temperature). Such transition is very similar to that seen in CFRO as a function of temperature on cooling[47].

The lack of a structural transition induced by applied pressure in BFRO is rather surprising, since chemical pressure induced by replacing Ba with Ca in BFRO stabilizes a monoclinic phase[78]. A small tetragonal distortion was reported in BFRO below the magnetic ordering temperature T_c=305 K in ambient-pressure high-resolution XRD measurements, reaching a maximum $c/a = 0.9984$ at T=14 K[50]. Our room temperature data do not show clear evidence for a tetragonal distortion in BFRO to the highest pressure measured. At low pressures below 10 GPa, where pressure gradients in the 4:1 Methanol:Ethanol pressure medium are small, undetected tetragonality is likely a result of insufficient angular resolution in the current measurements. At high-pressure, a clear broadening of XRD peaks occurs due to non-hydrostaticity of the pressure medium. The (400) full width half maximum (FWHM) reaches $\sim 0.2^\circ$ at 31 GPa. If we estimate our angular resolution to be half of this FWHM, then our data puts lower and upper bounds on unresolved tetragonality of $0.992 \lesssim c/a \lesssim 1.008$.

The relationship between the low-temperature coercivity and the room temperature lattice volume is plotted in Figure 7. The monoclinic structure of CFRO is approximated into a pseudo-cubic lattice in order to directly compare it with the cubic BFRO structure. We have also included in this figure coercivity changes with chemical pressure (P= 1 bar, 5 K) reported in Ref. 78. Volume compression increases the coercivity in a roughly linear fashion both for *chemical* and *physical* pressure. However, volume itself is not a predictor of coercivity. For example, the pre-compressed CFRO structure at ambient pressure (V ≈ 460Å^3) is less coercive ($H_c \sim 3$ kOe = 0.3 T) than the BFRO structure at 25 GPa with a similar volume ($H_c \sim 1.4$ T). This is still the case even if one compares to the higher coercivity values of CFRO reported at ambient pressure in Refs.[47,78] ($H_c \sim 9$ kOe), also included in Fig. 7. Nevertheless, a similar $\Delta H_c/\Delta V \sim$ 160-200 Oe/Å^3 is obtained for both samples. The similar-

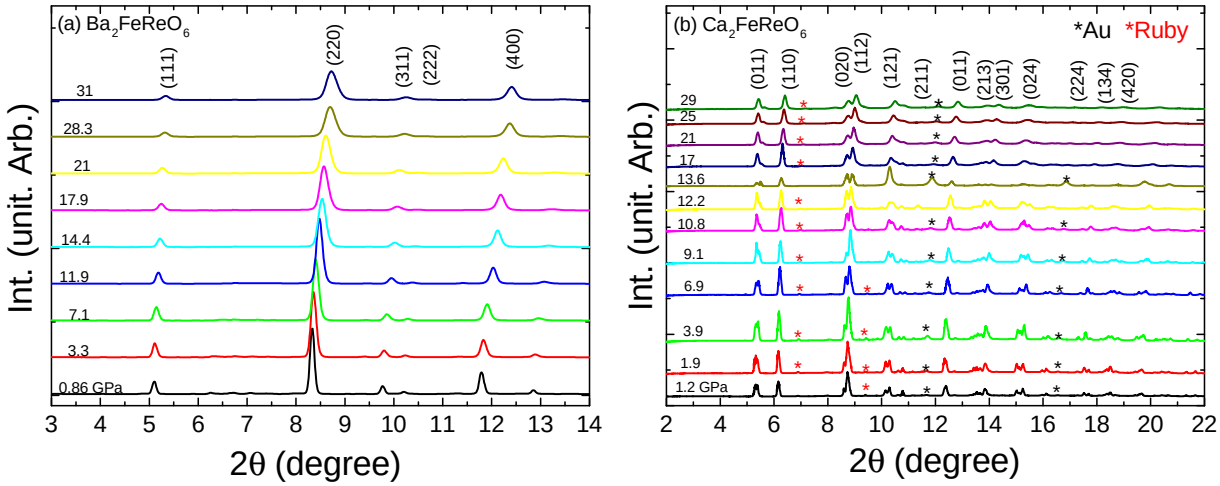

FIG. 5: X-ray powder diffraction data as a function of pressure for (a) BFRO and (b) CFRO collected at room temperature.

ity of $\Delta H_c/\Delta V$ points to an intrinsic origin of magnetic anisotropy upon volume compression. This is important since coercivity can have extrinsic contributions, such as a result of pinning of magnetic domain walls by defects.

The magnetic coercivity can also be modified by tunning the single ion anisotropy acting on the d orbitals. Such anisotropy is commonly a consequence of tetragonal crystal fields that split the d manifold creating easy/hard magnetic axis. In fact, the large increase in the coercivity of CFRO on cooling has been partially attributed to a change in the tetragonal distortion of ReO_6 octahedra[47] which changes from c-axis compressed to [110]/[1-10]-axis elongated[86] [see insets of Fig. 6 (c)]. Based solely on the lattice constants, the same change in tetragonality appears to occur under pressure at room temperature (Figs. 6 (c) and (d)). Therefore, while we do not have direct information on the pressure dependence of the structure at low temperature, our data implies that high-pressure favors the creation of ab-plane elongated octahedra much like cooling does. We note that there have been reports of phase separation/coexistence in CFRO at low temperature, although the literature remains ambiguous. Granado *et. al.*[32] report coexistence of monoclinic phases below 160 K, and that magnetic fields below 7 T can have an effect on their relative phase fraction (from 40-60% in zero field to 60-40% at 5 T). Westerburg *et. al.*[46] also reported coexistence of monoclinic phases, but below 400 K. This phase separation, which persists at low T, leads to highly unusual hysteresis loops at 10 K composed of magnetically hard and soft components each attributed to one of the coexisting monoclinic phases. Oikawa *et. al.*[47], on the other hand, report a single monoclinic phase at low T and square-shaped hysteresis loops. Our hysteresis loops at low T are square-shaped as well with similar remanence (M_r) to saturation (M_s) ratio to those in Ref.[47]. While we cannot rule out coexisting monoclinic phases with similar volumes and similar magnetic properties at low temperature, coexistence of magnetically soft/hard monoclinic phases as reported in Ref.[46] would have resulted in odd-shape hysteresis loops. Similarly, one may be tempted to argue that if coexistence of magnetically soft/hard phases takes place in CFRO at low T, that pressure may stabilize the magnetically hard phase explaining the increase in coercivity. However, this would lead to changes in the shape of the hysteresis loop under pressure, particularly in the M_r/M_s ratio, which is not observed. Note that a magnetic field of 4 T used in our low T experiments would only have a small effect on the relative fraction of coexisting phases[32]. Also, pulsed-field XMCD experiments[45] show that fields up to 10 T have a negligible effect on phase separation at low T, as seen by a constant m_l/m_s ratio. Finally, the similar $\Delta H_c/\Delta V$ for CFRO and BFRO shown in Fig. 7 is an additional indication that the mechanism behind the coercivity increase with pressure in CFRO is unrelated to pressure-tuning of volume fraction of coexisting phases at low T, as phase separation has not been reported for BFRO.

Figure 8 displays how degree of tetragonality correlates with the enhanced coercivity in CFRO as a function of both temperature and pressure. It is important to note that temperature-driven fluctuations can strongly affect magnetic domain dynamics, magnetization reversal, and coercivity, an effect that cannot be easily deconvolved. Despite this issue, Figure 8 does support the notion that tetragonal distortion of ReO_6 octahedra is a leading cause for the observed change in coercivity.

That no tetragonal distortion is evident in the diffrac-

tion pattern of the BFRO sample to the highest pressures measured is puzzling since its coercivity is largely enhanced (Fig. 7). Assuming a tetragonal distortion is the only contributor to coercivity, interpolating the coercivity of BFRO into the coercivity vs. tetragonality relation of CFRO (Fig. 8) would lead to a tetragonal distortion of ReO_6 octahedra in BFRO $d[Re-O_{apical}]/d[Re-O_{equatorial}] \sim 1.02$ at 26 GPa. This distortion would drive an increase in c/a ratio of ~ 1.01, which is marginally larger than our estimated sensitivity ($0.992 \lesssim c/a \lesssim 1.008$). Therefore, unresolved tetragonality in BFRO can still be the primary driver behind its increased coercivity, in line with results for CFRO. We note, however, that unlike CFRO, BFRO displays a c-axis compression of the ReO_6 octahedra at low temperature ($d[Re-O_{apical}]/d[Re-O_{equatorial}] \sim 0.9984$)[32]. Therefore it is unclear what kind of tetragonal distortion occurs in BFRO at both low temperature and high pressures. High-resolution low-temperature x-ray diffraction measurements are needed to address this issue.

C. Magnetic anisotropy within j_{eff} model

In order to obtain an estimate of the effect of a tetragonal distortion on the magnetic anisotropy, we employ the same model as in Section III B describing a rhenium ion in the presence of a spin-orbit interaction and cubic and tetragonal crystal fields. To obtain the correct ground state, an exchange field Δ_{exch} acting on the spins was introduced resulting in an interaction $\mathbf{S} \cdot \Delta_{\text{exch}}$. This field mimics the Hund's Coulomb exchange interaction and ensures that the lowest configuration is $e' \uparrow e''_+ \uparrow$. The use of an exchange field allows us to set up an effective one-particle Hamiltonian H. The 10×10 matrix for the ten $5d$ orbitals is solved numerically. The ground-state energy is then given by $E_0 = \langle e' \uparrow |H| e' \uparrow \rangle + \langle e''_+ \uparrow |H| e''_+ \uparrow \rangle$. The

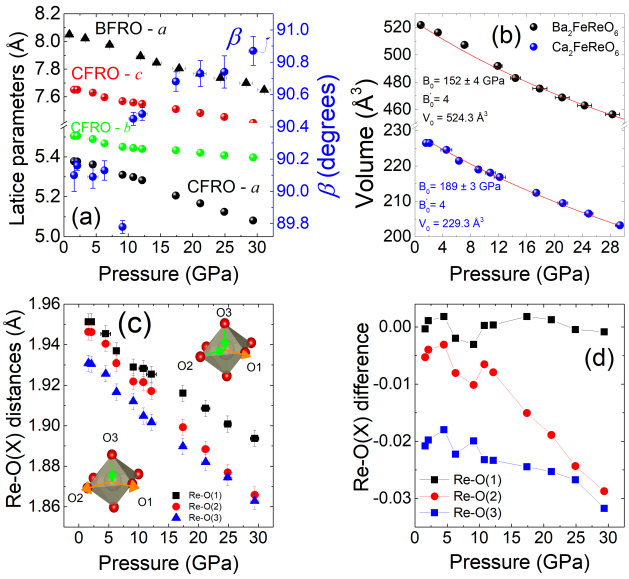

FIG. 6: (a) Pressure-dependent lattice parameters for BFRO and CFRO, (b) unit cell volume together with fits to a second-order B-M equation used to obtain bulk moduli from the measured P-V relationships, (c) pressure dependence of Re-O distances in ReO_6 octahedra with insets illustrating evolution of tetragonal distortion from c-axis compressed at low pressure to in-plane elongated at high pressure, and (d) variation of Re-O distances with pressure relative to basal plane Re-O(1) distance.

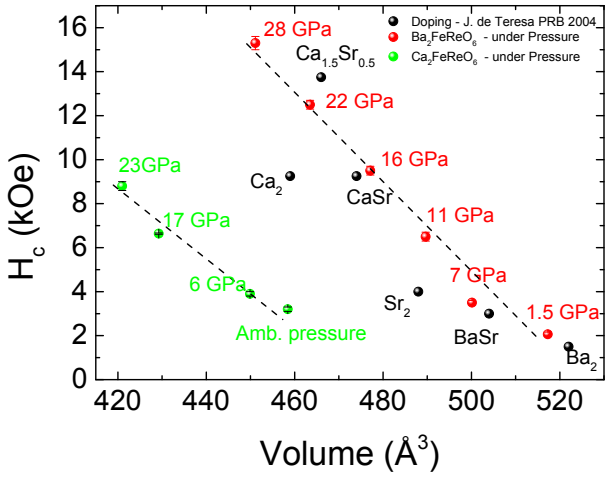

FIG. 7: Coercivity as function of cubic (BFRO) and pseudocubic (CFRO) unit cell volume driven by applied pressure (T=10K, this study) compared to coercivity changes with chemical pressure (T=5 K, ambient pressure) in $Ca_xSr_{2-x}FeReO_6$ and $Sr_{2-y}Ba_yFeReO_6$ samples with $x, y = 0$, 0.5, 1, 1.5 and 2[78].

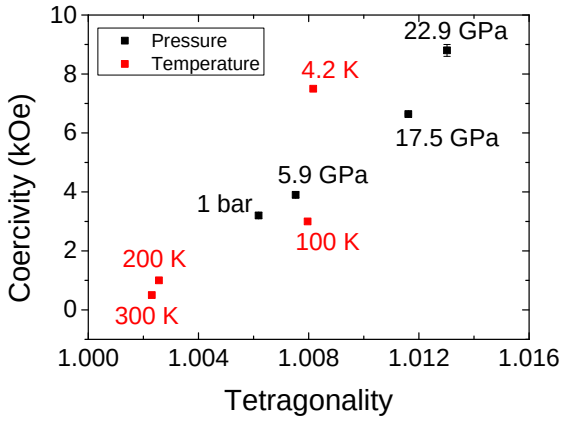

FIG. 8: Coercivity as a function of the [1±10]-oriented tetragonal elongation. The tetragonality is defined as the ratio between Re-O1 and the average of Re-O2 and Re-O3. The temperature dependence was extracted from the literature[47].

direction of the local moment with respect to the crystal axes can be changed by a magnetic field. In the absence of a tetragonal distortion, the ground-state energy of the $e' \uparrow e''_+ \uparrow$ configuration is independent of the direction of the spin, *i.e.* the energy does not depend on the direction of the moment. This is comparable to two electrons in essentially spherically-symmetric $j_{\rm eff} = \frac{3}{2}$ states. This is no longer the case when a tetragonal field is applied causing a splitting ε_{xy} between the xy and yz/zx orbitals. We take ε_{xy} smaller than the strength of the spin-orbit interaction ζ, see Fig. 2. The change in energy as a function of the direction of the moment is solely due to the e'' states since the e' states are not affected by the tetragonal distortion. The tetragonal distortion mixes the e''_+ and e''_- states, thereby coupling the two $j_{\rm eff}$ states. The energy of the e''_+ state can only change when the character of the wavefunction is affected by the direction of the moment. This is only possible by coupling it to the e''_- state. The calculated dependence of the energy on the angle of the magnetic moment θ_m with respect to the z axis is given by the dots in Fig. 9.

In the limit that $10Dq$ is much larger than all the other parameters, the θ_m dependence can be well modeled by

$$E_0 = K_0 + K_1 \sin^2 \theta_m, \tag{13}$$

as expected for a system with uniaxial anisotropy and as verified by the results from explicit numerical calculation shown in Fig. 9. K_0 is a simple shift and not important for the anisotropy. By varying their values, the dependence of K_1 on the parameters can be determined. Numerically, the dependence on the parameters can be determined to be

$$K_1 \cong -0.45 \frac{\Delta_{\rm exch} \varepsilon_{xy}}{\zeta}, \tag{14}$$

in the limit $\varepsilon_{xy} \ll \Delta_{\rm exch} \ll \zeta \ll 10Dq$, which is the expected hierarchy of energy scales for the Rhenium ion. When the parameter values are closer together, the expression for K_1 becomes less accurate, but still describes rather well the trends when changing the parameter values. Note that the energy difference between the moment in- ($\theta_m = 90°$) and out of the plane ($\theta_m = 0°$) increases when $\varepsilon_{xy} < 0$.

This theoretical analysis naturally explains the correlation between coercivity and ReO_6 tetragonality. Noticeably, equations 13 and 14 imply that a reduction of effective spin-orbit coupling could cooperate with a tetragonal distortion in driving the increased coercivity. This occurs because spin-orbit coupling effectively mixes the $|xy\rangle$, $|yz\rangle$ and $|zx\rangle$ wavefunctions, reducing the single-ion anisotropy. This effect, if present, could be more significant in BFRO than CFRO since our XANES results show a reduction in BR with pressure in this sample (see Table I). Since a reduction in ζ affects the separation between $j_{\rm eff}$ manifolds, this hypothesis could be verified with Re L-edge resonant inelastic x-ray scattering experiments at high-pressure. Finally, local Jahn-Teller (J-T) distortions of ReO_6 octahedra, which could become active for a Re d^2 configuration, may contribute to anisotropy and remain undetected in our XRD measurements if they fail to order at room temperature. A description of the J-T effect in the presence of strong spin-orbit coupling in $j_{\rm eff} = \frac{3}{2}$ orbitals is outside the scope of this paper. That the tetragonal energy depends on the spin direction is indicative of magneto-elastic coupling, an effect reported for BFRO in Ref. 85.

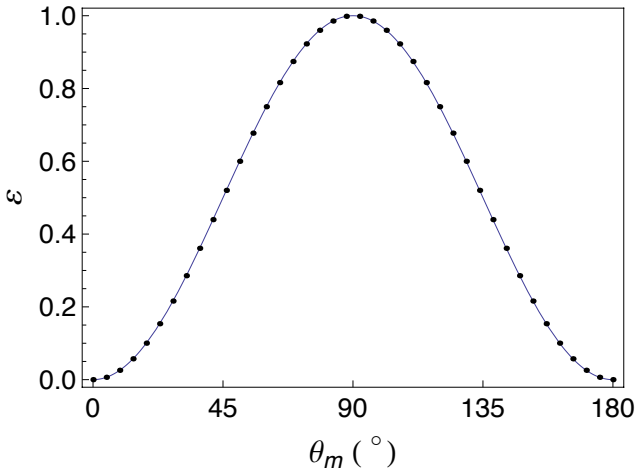

FIG. 9: The dots give the calculated expectation value of the normalized ground-state energy, $\varepsilon = (E_0(\theta_m) - E_0(0°))/(E_0(90°) - E_0(0°))$, as a function of the angle θ_m of the magnetic moment with respect to the z axis calculated using the $j_{\rm eff}$ model. The solid line gives a $\sin^2 \theta_m$ fit to the calculated values

V. SUMMARY

XMCD experiments under quasi-hydrostatic pressure conditions show remarkable enhancement of magnetic hardness with volume compression in both BFRO and CFRO powder samples. The rate of coercivity increase with volume reduction is similar for both samples. The unquenched orbital moment in Re $5d$ orbitals determined from XMCD sum rules does not increase with pressure. The enhanced single ion anisotropy under pressure appears to arise from an increased tetragonal distortion of ReO_6 octahedra. This distortion is quantified in the monoclinic CFRO sample and scales linearly with the coercivity. Limited resolution in the XRD data of the BFRO sample only allowed placing an upper limit on the size of the distortion. A $j_{\rm eff}$ theoretical description of the Re $5d^2$ orbitals is developed to interpret the spectroscopic data pointing to a Hund's rule like "high spin" ground state with two electrons in crystal-field split $j_{\rm eff} = \frac{3}{2}$ states. A derivation of the magnetic anisotropy of Re $5d^2$ states within this model yields the counterintuitive result that a reduction in the strength of the effective spin-orbit interaction at high pressures may cooperate with a tetragonal

distortion in enhancing the Re $5d$ anisotropy.

Acknowledgments

Work at Argonne is supported by the U.S. Department of Energy, Office of Science, Office of Basic Energy Sciences, under Contract No. DE-AC-02-06CH11357. HP-CAT operations are supported by the U.S. DOE National Nuclear Security Administration (NNSA) under Award No. DE-NA0001974 and DOE Basic Energy Sciences (BES) under Award No. DE-FG02-99ER45775, with partial instrumentation funding by National Science Foundation (NSF). C.A.E.Jr. is supported by FAPESP (P-Brazil) under contract No. 2016/24137-3. M.v.V is supported by the U.S. Department of Energy (DOE), Office of Basic Energy Sciences, Division of Materials Sciences and Engineering under Award No. DE-FG02-03ER46097. We also thank GSECARS for use of laser drilling facilities. J. G. thanks NASI, Allahabad, India, for the award of a Senior Scientist Fellowship.

Appendix A: Dichroic intensities

For the sum rules of the dichroic spectra, we need to consider expectation values of different operators. The coupled tensors can be written as[73] w_ζ^{xyz}, where a tensor of rank x operating on the orbital is coupled to a tensor of rank y operating on the spin to form a total tensor of rank z. The angular momentum is given by $L_q = 2w_q^{101}$, whose orbital part is a vector (a tensor of rank 1, *i.e.* $x = 1$). Since the tensor with $y = 0$ operating on the spin is the identity matrix, the total operator is also a vector ($z = 1$) and equal to the tensor working on the orbital. In the same fashion, we can define the spin operator, which is a tensor that only works on the orbital, $S_q = \frac{1}{2}w_q^{011}$. The simplest tensor that combines both orbital and spin parts is $\mathbf{L}\cdot\mathbf{S} = w_q^{110}$ which gives the inner product ($z = 0$) of the orbital ($x = 1$) and spin ($y = 1$) momentum or the spin-orbit coupling. However, this coupled tensor is a scalar and of importance for the sum rules for isotropic spectra, see Eq. (11). For magnetic effects, an additional tensor of rank $z = 1$, *i.e.* a vector, is needed. The relevant operator is w_q^{211}, also known as the magnetic dipole moment. This couples a quadrupolar ($x = 2$) operator working on the orbital part with the spin ($y = 1$) to form a total coupled tensor of rank $z = 1$. With the expressions for the eigenstates in the main text, we can evaluate the ground-state expectation values of the operators relevant for the sum rules for magnetic dichroism[64,65].

Using the wavefunctions for the $j_{\rm eff}$ states in Eqs. (2), (4) and (5), the expectation value for the angular momentum L_z can be straightforwardly calculated since only the $|\pm 1,\sigma\rangle$, states where σ is the spin, contribute to the angular momentum. For the $j_{\rm eff} = \frac{1}{2}$ state, the expectation value is $\langle L_z\rangle_{e''_-,\pm\frac{1}{2}} = \mp\cos^2\theta = \mp\frac{2}{3} \rightarrow \mp 1$, giving the values for the tetragonal field $|\varepsilon_{xy}| = 0 \rightarrow \infty$ (always under the assumption that $|\varepsilon_{xy}| \ll 10Dq$). These values show the limits for $|\varepsilon_{xy}| \ll \zeta$ and $|\varepsilon_{xy}| \gg \zeta$, where ζ is the strength of the spin-orbit interaction. Therefore, the angular momentum of the $j_{\rm eff} = \frac{1}{2}$ state is enhanced by the tetragonal field. However, although this can be of importance for iridates, for the rhenium oxides, these states are empty and therefore do not contribute to the angular momentum. The corresponding $j_{\rm eff} = \frac{3}{2}$ state of the same symmetry has an angular momentum $\langle L_z\rangle_{e''_+,\pm\frac{1}{2}} = \mp\sin^2\theta = \mp\frac{1}{3} \rightarrow 0$ for $|\varepsilon_{xy}| = 0 \rightarrow \infty$. Here, the angular momentum is quenched by the tetragonal field. The other $j_{\rm eff} = \frac{3}{2}$ state gives $\langle L_z\rangle_{e',\pm\frac{1}{2}} = \mp 1$, *i.e.* opposite to the spin component and is independent of the tetragonal field.

The spin momentum is given by $S_q = \frac{1}{2}w_q^{011}$. For the $j_{\rm eff} = \frac{1}{2}$ state, the expectation value of the spin $\langle S_z\rangle_{e''_-,\pm\frac{1}{2}} = \mp\frac{1}{2}\cos 2\theta = \mp\frac{1}{6} \rightarrow \mp\frac{1}{2}$ is opposite to the spin component of e''_-. For e''_+, the opposite is found $\langle S_z\rangle_{e''_+,\pm\frac{1}{2}} = \pm\frac{1}{2}\cos 2\theta = \pm\frac{1}{6} \rightarrow \pm\frac{1}{2}$. For the other $j_{\rm eff} = \frac{3}{2}$ states, the expectation value is equal to the spin component, $\langle S_z\rangle_{e',\pm\frac{1}{2}} = \pm\frac{1}{2}$.

The third tensor of rank one of importance to the x-ray dichroism sum rules is the magnetic dipole moment w^{211}. Although often argued to be small, this assumption is incorrect for materials where the spin-orbit interaction plays an important role. The diagonal matrix element of this operator is given by $\sigma(2 - 3m_{\rm eff}^2)$, taking $m_{\rm eff} = 0$ for the xy orbital. This directly gives the expectation values $\langle w_z^{211}\rangle_{e',\pm\frac{1}{2}} = \mp\frac{1}{2}$. The evaluation of the other eigenstates is somewhat more involved due to off-diagonal matrix elements. The other $j_{\rm eff} = \frac{3}{2}$ states have a magnetic dipole moment $\langle w_z^{211}\rangle_{e''_+,\pm\frac{1}{2}} = \pm[\frac{3}{4} + \frac{1}{4}\cos 2\theta + 3\sin 2\theta/(2\sqrt{2})] = \pm\frac{11}{6} \rightarrow \pm 1$. The value ± 1 is the magnetic dipole moment of the $|xy,\pm\frac{1}{2}\rangle$ orbital. The $j_{\rm eff} = \frac{1}{2}$ state has a magnetic dipole moment $\langle w_z^{211}\rangle_{e''_-,\pm\frac{1}{2}} = \pm[\frac{3}{4} - \frac{1}{4}\cos 2\theta - 3\sin 2\theta/(2\sqrt{2})] = \mp\frac{1}{3} \rightarrow \pm\frac{1}{2}$.

Inserting the values of the coupled tensors in Eq. (6) allows the calculation of the dichroic absorption intensity at a particular spin-orbit split edge for each of the orbitals. These results are given in Eq. (7)

* Current address: CSIR-Central Electrochemical Research Institute, Madras Unit, Chennai, India

† Electronic address: veenendaal@niu.edu

‡ Electronic address: haskel@aps.anl.gov

[1] S. Vasala and M. Karppinen, Prog. Solid State Chem. **43**, 1 (2015).
[2] D. Serrate, J. M. D. Teresa, and M. R. Ibarra, J. Phys. Cond. Matter **19**, 023201 (2006).
[3] A. S. Bhalla, R. Guo, and R. Roy, Mater. Res. Innovat. **4**, 3 (2000).
[4] V. N. Antonov, L. V. Bekenov, and A. Ernst, Phys. Rev. B **94**, 035122 (2016).
[5] A. W. Sleight, J. Longo, and R. Ward, Inorg. Chem. **1**, 245 (1962).
[6] M. G. Blamire, J. L. MacManus-Driscoll, N. D. Mathur, and Z. H. Barber, Adv. Mater. **21**, 3827 (2009).
[7] M. Anderson, K. Greenwood, G. Taylor, and K. Poeppelmeier, Prog. Solid State Chem. **22**, 197 (1993).
[8] P. Majewski, S. Geprags, O. Sanganas, M. Opel, R. Gross, F. Wilhelm, A. Rogalev, and L. Alff, Appl. Phys. Lett. **87**, 3 (2005).
[9] C. Khattak, D. Cox, and F. Wang, J. Solid State Chem. **13**, 77 (1975).
[10] K.-I. Kobayashi, T. Kimura, Y. Tomioka, H. Sawada, K. Terakura, and Y. Tokura, Phys. Rev. B **59**, 11159 (1999).
[11] H. Wu, Phys. Rev. B **64**, 125126 (2001).
[12] G. Vaitheeswaran, V. Kanchana, and A. Delin, Appl. Phys. Lett. **86**, 032513 (2005).
[13] H.-T. Jeng and G. Y. Guo, Phys. Rev. B **67**, 094438 (2003).
[14] S. Ali, W. Khan, G. Murtaza, M. Yaseen, S. Ramay, and A. Mahmood, J. Mag. Magn. Mater. **441**, 113 (2017).
[15] R. Das, G. P. Das, and S. K. Srivastava, **49** (2016).
[16] M. Musa Saad H.E., Chem. Phys. **483**, 35 (2017).
[17] P. W. Anderson, Phys. Rev. **79**, 350 (1950).
[18] J. B. Goodenough, Phys. Rev. **100**, 564 (1955).
[19] J. B. Goodenough, J. Phys. Chem. Solids **6**, 287 (1958).
[20] J. Kanamori, J. Phys. Chem. Solids **10**, 87 (1959).
[21] H. L. Feng, M. Arai, Y. Matsushita, Y. Tsujimoto, Y. Guo, C. I. Sathish, X. Wang, Y. H. Yuan, M. Tanaka, and K. Yamaura, J. Am. Chem. Soc. **136**, 3326 (2014).
[22] R. Morrow, J. Yan, M. A. McGuire, J. W. Freeland, D. Haskel, and P. M. Woodward, Phys. Rev. B **92**, 094435 (2015).
[23] K. Rolfs, S. Toth, E. Pomjakushina, D. Sheptyakov, J. Taylor, and K. Conder, Phys. Rev. B **91**, 5 (2015).
[24] R. Morrow, K. Samanta, T. Saha Dasgupta, J. Xiong, J. W. Freeland, D. Haskel, and P. M. Woodward, Chem Mater. **28**, 3666 (2016).
[25] X. Zhang, B. Grabowski, F. Körmann, C. Freysoldt, and J. Neugebauer, Phys. Rev. B **95**, 165126 (2017), ISSN 2469-9950.
[26] M. Sigalas, D. A. Papaconstantopoulos, and N. C. Bacalis, Phys. Rev. B **45**, 5777 (1992).
[27] M. S. Moreno, J. E. Gayone, M. Abbate, A. Caneiro, D. Niebieskikwiat, R. D. Sánchez, A. De Siervo, R. Landers, and G. Zampieri, Physica B **320**, 43 (2002).
[28] O. Erten, O. N. Meetei, A. Mukherjee, M. Randeria, N. Trivedi, and P. Woodward, Phys. Rev. B **87**, 1 (2013).
[29] T. Alamelu, U. V. Varadaraju, M. Venkatesan, A. P. Douvalis, and J. M. D. Coey, J. Appl. Phys. **91**, 8909 (2002).
[30] M. Sikora, C. Kapusta, M. Borowiec, C. J. Oates, V. Prochazka, D. Rybicki, D. Zajac, J. M. De Teresa, C. Marquina, and M. R. Ibarra, Appl. Phys. Lett. **89**, 062509 (2006).
[31] D. Serrate, J. M. De Teresa, P. A. Algarabel, C. Marquina, L. Morellon, J. Blasco, and M. R. Ibarra, J. Mag. Magn. Mater. **290**, 843 (2005).
[32] E. Granado, Q. Huang, J. W. Lynn, J. Gopalakrishnan, R. L. Greene, and K. Ramesha, Phys. Rev. B **66**, 064409 (2002).
[33] A. A. Aczel, Z. Zhao, S. Calder, D. T. Adroja, P. J. Baker, and J.-Q. Yan, Phys. Rev. B **93**, 214407 (2016).
[34] H. Kato, T. Okuda, Y. Okimoto, Y. Tomioka, K. Oikawa, T. Kamiyama, and Y. Tokura, Phys. Rev. B **65**, 144404 (2002).
[35] S. Wurmehl and J. T. Kohlhepp, J. Phys. D **41** (2008).
[36] C. A. Vaz, J. Phys. Cond. Matter **24** (2012).
[37] M. Opel, J. Phys. D **45** (2012).
[38] Y. Zhang, L. Duan, and V. Ji, Surf Interf Anal **49**, 960 (2017).
[39] G. Popov, M. Greenblatt, and M. Croft, Phys. Rev. B **67**, 024406 (2003).
[40] D. Zajac, M. Sikora, V. Prochazka, M. Borowiec, J. Stepien, C. Kapusta, P. C. Riedi, C. Marquina, J. M. De Teresa, and M. R. Ibarra, Acta Physica Polonica A **111**, 797 (2007).
[41] N. Rammeh, K. G. Bramnik, H. Ehrenberg, C. Ritter, H. Fuess, and A. Cheikh-Rouhou, Phys. Stat. Sol. (c) **1**, 1669 (2004).
[42] W. Prellier, V. Smolyaninova, A. Biswas, C. Galley, R. L. Greene, K. Ramesha, and J. Gopalakrishnan, J. Phys. Cond. Matt. **12**, 965 (2000).
[43] J. Gopalakrishnan, A. Chattopadhyay, S. B. Ogale, T. Venkatesan, R. L. Greene, A. J. Millis, K. Ramesha, B. Hannoyer, and G. Marest, Phys. Rev. B **62**, 9538 (2000).
[44] S. Gong, S.-D. Guo, P. Chen, and B.-G. Liu, RSC Adv. **5**, 63165 (2015).
[45] M. Sikora, O. Mathon, P. van der Linden, J. M. Michalik, J. M. de Teresa, C. Kapusta, and S. Pascarelli, Phys. Rev. B **79**, 220402 (2009).
[46] W. Westerburg, O. Lang, C. Ritter, C. Felser, W. Tremel, and G. Jakob, Solid State Comm. **122**, 201 (2002).
[47] K. Oikawa, T. Kamiyama, H. Kato, and Y. Tokura, J. Phys. Soc. Jpn **72**, 1411 (2003).
[48] N. Auth, G. Jakob, W. Westerburg, C. Ritter, I. Bonn, C. Felser, and W. Tremel, J. Mag. Magn. Mater. **272**, E607 (2004).
[49] S. Nakamura, M. Tanaka, H. Kato, and Y. Tokura, J. Phys. Soc. Jpn **72**, 424 (2003).
[50] C. Azimonte, J. C. Cezar, E. Granado, Q. Huang, J. W. Lynn, J. C. P. Campoy, J. Gopalakrishnan, and K. Ramesha, Phys. Rev. Lett. **98**, 017204 (2007).
[51] F. F. Ferreira, E. Granado, W. Carvalho, S. W. Kycia, D. Bruno, and R. Droppa, J. Synch. Rad. **13**, 46 (2006).
[52] A. Cook and A. Paramekanti, Phys. Rev. B **88**, 1 (2013).
[53] C. Azimonte, E. Granado, J. C. Cezar, J. Gopalakrishnan, and K. Ramesha, J. Appl. Phys. **101**, 09H115 (2007).
[54] D. Haskel, Y. C. Tseng, J. C. Lang, and S. Sinogeikin, Rev. Sci. Instrum. **78**, 083904 (2007).
[55] J. C. Lang and G. Srajer, Rev. Sci. Instrum. **66**, 1540 (1995).
[56] M. Suzuki, Y. Inubushi, M. Yabashi, and T. Ishikawa, J. Synch. Rad. **21**, 466 (2014).
[57] K. Hirano, K. Izumi, T. Ishikawa, S. Annaka, and S. Kikuta, Jpn. J. Appli. Phys. **30**, L407 (1991).
[58] D. Haskel, Y. Tseng, N. Souza-Neto, J. Lang, S. Sinogeikin, Y. Mudryk, K. Gschneidner Jr., and V. Pecharsky, High Pressure Research **28** (2008).
[59] G. J. Piermarini, S. Block, J. D. Barnett, and R. A. Forman, J. Appl. Phys. **46**, 2774 (1975).
[60] M. S. Torikachvili, S. K. Kim, E. Colombier, S. L. Bud'ko, and P. C. Canfield, Review of Scientific Instruments **86**,

123904 (2015).
[61] A. L. Bail, H. Duroy, and J. L. Fourquet, Mater. Res. Bull. **23**, 447 (1988).
[62] B. H. Toby and R. B. Von Dreele, J. Appl. Crystallogr. **46**, 544 (2013).
[63] C. T. Chen, Y. U. Idzerda, H.-J. Lin, N. V. Smith, G. Meigs, E. Chaban, G. H. Ho, E. Pellegrin, and F. Sette, Phys. Rev. Lett. **75**, 152 (1995).
[64] B. T. Thole, P. Carra, F. Sette, and G. van der Laan, Phys. Rev. Lett. **68**, 1943 (1992).
[65] P. Carra, B. T. Thole, M. Altarelli, and X. Wang, Phys. Rev. Lett. **70**, 694 (1993).
[66] A. Sleight and J. Weiher, J. Phys. Chem. Solids **33**, 679 (1972).
[67] G. Jackeli and G. Khaliullin, Phys. Rev. Lett. **102**, 017205 (2009).
[68] A. Winkler, N. Narayanan, D. Mikhailova, K. G. Bramnik, H. Ehrenberg, H. Fuess, G. Vaitheeswaran, V. Kanchana, F. Wilhelm, A. Rogalev, et al., New J. Phys. **11**, 073047 (2009).
[69] J. P. Crocombette, B. T. Thole, and F. Jollet, J. Phys.:Condens. Matter **8**, 4095 (1996).
[70] C. Kapusta, D. Zając, P. Riedi, M. Sikora, C. Oates, J. Blasco, and M. Ibarra, J. Mag. Magn. Mater. **272**, E1619 (2004).
[71] P. Majewski, S. Gepräs, O. Sanganas, M. Opel, R. Gross, F. Wilhelm, A. Rogalev, and L. Alff, Appl. Phys. Lett. **87**, 202503 (2005).
[72] J. S. Griffith, *The Theory of Transition-Metal Ions* (Cambridge University Press, Cambridge, 1961).
[73] M. van Veenendaal, *The Theory of Inelastic Scattering and Absorption of X-rays* (Cambridge University Press, Cambridge, 2015).
[74] B. T. Thole and G. van der Laan, Phys. Rev. B **38**, 3158 (1988).
[75] M. A. Laguna-Marco, D. Haskel, N. Souza-Neto, J. C. Lang, V. V. Krishnamurthy, S. Chikara, G. Cao, and M. van Veenendaal, Phys. Rev. Lett. **105**, 216407 (2010).
[76] D. Haskel, G. Fabbris, M. Zhernenkov, P. P. Kong, C. Q. Jin, G. Cao, and M. van Veenendaal, Phys. Rev. Lett. **109**, 027204 (2012).
[77] S. Chikara, D. Haskel, J.-H. Sim, H.-S. Kim, C.-C. Chen, G. Fabbris, L. S. I. Veiga, N. M. Souza-Neto, J. Terzic, K. Butrouna, et al., Phys. Rev. B **92**, 081114 (2015).
[78] J. M. De Teresa, D. Serrate, J. Blasco, M. R. Ibarra, and L. Morellon, Phys. Rev. B **69**, 144401 (2004).
[79] B. G. Kim, Y. S. Hor, and S. W. Cheong, Appl. Phys. Lett. **79**, 388 (2001).
[80] H. Kato, T. Okuda, Y. Okimoto, Y. Tomioka, K. Oikawa, T. Kamiyama, and Y. Tokura, Phys. Rev. B **69**, 184412 (2004).
[81] F. Birch, J. Geophys. Res. **83**, 1257 (1978).
[82] R. Jeanloz, Geophys. Res. Lett. **8**, 1219 (1981).
[83] S. Meenakshi, V. Vijayakumar, S. N. Achary, and A. K. Tyagi, J. Phys. Chem. Solids **72**, 609 (2011).
[84] D. D. Han, W. Gao, N. N. Li, R. L. Tang, H. Li, Y. M. Ma, Q. L. Cui, P. W. Zhu, and X. Wang, Chin. Phys. B **22** (2013).
[85] A. F. García-Flores, A. F. L. Moreira, U. F. Kaneko, F. M. Ardito, H. Terashita, M. T. D. Orlando, J. Gopalakrishnan, K. Ramesha, and E. Granado, Phys. Rev. Lett. **108**, 177202 (2012).
[86] The low temperature phase of CFRO features elongated ReO_6 octahedra in which the tetragonal axis alternates between [110] and [1-10] orientations[47].